

DOI: [10.29026/oea.2025.250025](https://doi.org/10.29026/oea.2025.250025)CSTR: [32247.14.oea.2025.250025](https://cstr.net/urn:nid:CN=32247.14.oea.2025.250025)

# Embedded solar adaptive optics telescope: achieving compact integration for high-efficiency solar observations

Naiting Gu<sup>1\*</sup>, Hao Chen<sup>2,3</sup>, Ao Tang<sup>2,3,4</sup>, Xinlong Fan<sup>2,3</sup>,  
Carlos Quintero Noda<sup>5,6</sup>, Yawei Xiao<sup>2,3,4</sup>, Libo Zhong<sup>2,3</sup>, Xiaosong Wu<sup>2,3,4</sup>,  
Zhenyu Zhang<sup>3</sup>, Yanrong Yang<sup>7</sup>, Zao Yi<sup>8</sup>, Xiaohu Wu<sup>9\*</sup>, Linhai Huang<sup>2,3,4\*</sup>  
and Changhui Rao<sup>2,3,4\*</sup>

<sup>1</sup>College of Advanced Interdisciplinary Studies, National University of Defense Technology, Changsha 410073, China; <sup>2</sup>National Laboratory on Adaptive Optics, Chengdu 610209, China; <sup>3</sup>Institute of Optics and Electronics, Chinese Academy of Sciences, Chengdu 610209, China; <sup>4</sup>University of Chinese Academy of Sciences, Beijing 101408, China; <sup>5</sup>Departamento de Astrofísica, Univ. De La Laguna, La Laguna, Tenerife E-38025, Spain; <sup>6</sup>Instituto de Astrofísica de Canarias, La Laguna, Tenerife E-38025, Spain; <sup>7</sup>Chengdu University of Traditional Chinese Medicine, Chengdu 610075, China; <sup>8</sup>Joint Laboratory for Extreme Conditions Matter Properties, Southwest University of Science and Technology, Mianyang 621010, China; <sup>9</sup>Thermal Science Research Center, Shandong Institute of Advanced Technology, Jinan 250100, China.

\*Correspondence: NT Gu, E-mail: [gnt7328@163.com](mailto:gnt7328@163.com); XH Wu, E-mail: [xiaohu.wu@iat.cn](mailto:xiaohu.wu@iat.cn); LH Huang, E-mail: [hlhai@ioe.ac.cn](mailto:hlhai@ioe.ac.cn); CH Rao, E-mail: [chrao@ioe.ac.cn](mailto:chrao@ioe.ac.cn)

## This file includes:

[Section 1: System overview and design of the 600 mm ESAOT prototype](#)

[Section 2: DSM and HS f-WFS design](#)

[Section 3: Experimental results](#)

Supplementary information for this paper is available at <https://doi.org/10.29026/oea.2025.250025>



**Open Access** This article is licensed under a Creative Commons Attribution 4.0 International License.

To view a copy of this license, visit <http://creativecommons.org/licenses/by/4.0/>.

© The Author(s) 2025. Published by Institute of Optics and Electronics, Chinese Academy of Sciences.

## Section 1: System overview and design of the 600 mm ESAOT prototype

The 600 mm prototype of the embedded solar adaptive optics telescope (ESAOT) is designed to validate the proposed methodology and system integration for high-precision photospheric imaging. The key system parameters are summarized in [Table S1](#).

**Table S1** | System parameters of the 600 mm ESAOT prototype.

Parameter	Value
Optical design	On-axis gregorian optics
Aperture size	$\Phi=600$ mm ( $\Phi=590$ mm clear aperture)
Obstruction ratio	35.6% (diameter)
Field of view (FoV)	$\sim\Phi 3'$
Spectral coverage	380–2500 nm
DSM profile	Concave ellipsoid
Mount	Equatorial type, DDM160 by ASA
Image space $F\#$	$\sim F/9$
Post-focus instruments	TiO band imager (first light), H $\alpha$ line and magnetic field imager (future)

The primary scientific objective of the ESAOT prototype is to achieve near-diffraction-limited imaging of the solar atmosphere, particularly focusing on active regions and their evolution in the photosphere. The optical design and system architecture are illustrated in [Fig. S1\(a\)](#) and [S1\(b\)](#). The system employs a single Gregorian optical configuration with an open tube truss to maintain precise alignment of optical components. The telescope is mounted on an equatorial DDM160 mount by ASA, Austria, and features a TiO<sub>2</sub>-coated sun shield to protect the truss from solar radiation. A heat-stop is positioned at the primary focus (F1) to mitigate thermal effects. A deformable secondary mirror (DSM) with 61 actuators is installed 300 mm behind the exit pupil. A fold mirror (FM) is placed above the primary mirror, directing light to the scientific focus (F2) and post-focus instruments mounted on the truss. The experimental configuration in [Fig. S1](#) incorporates a strategically re-positioned thermal control system located posterior to the primary mirror, with the science detector and HS f-WFS mounted laterally on the ESAOT structure. This spatial reallocation achieves optimized mass distribution for enhanced opto-mechanical stability, albeit introducing a measurable transmittance trade-off compared to the idealized schematic in [Fig. 1](#). While this represents the primary divergence between the two configurations, both architectures preserve identical operational principles. The [Fig. S1](#) implementation serves as a functionally equivalent testbed, intentionally retaining design flexibility to enable subsequent refinement toward the [Fig. 1](#) paradigm in operational deployments.

The post-focus instruments include an imaging detector and a Hartmann-shack full-wavefront sensor (HS f-WFS) for real-time measurement of wavefront aberrations. Initially, the system is equipped with a TiO band imager centered at 705.7 nm for photospheric observations. Future upgrades will include H $\alpha$  line and magnetic field imagers for chromospheric studies.

The 600 mm ESAOT prototype utilizes a two-mirror Gregorian system comprising a primary mirror (PM), a deformable secondary mirror (DSM), and a fold mirror (FM). The PM is a lightweight honeycomb structure made of ULE material, with a concave paraboloid surface and a focal length of 1020 mm. The DSM features a concave ellipsoid surface with a radius of 504.8 mm and a conic coefficient of  $-0.466$ . The FM is a flat mirror made of SiC. Detailed optical parameters are provided in [Table S2](#).

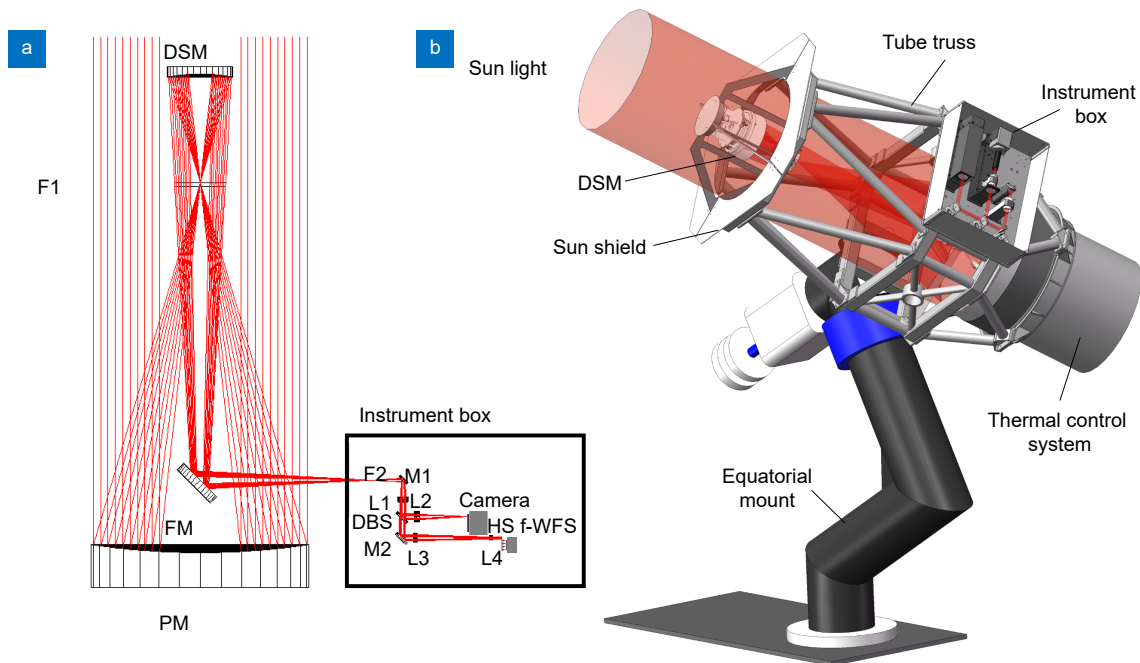


**Fig. S1** | 600 mm aperture ESAOT prototype. (a) Optical design of the 600 mm ESAOT prototype. (b) System architecture integrating a 61-actuator DSM and a 96-lenslet HS f-WFS for adaptive optics control. PM: Primary mirror; DSM: Deformable secondary mirror; FM: Fold mirror; DBS: Dichroic beam-splitter; F1: Primary focus; F2: Scientific focus; M1/2: Reflective mirror; L1: Collimator; L2: Imaging lens; L3&4: Beam shrink lenses; HS f-WFS: Hartmann-shack full-wavefront sensor.

**Table S2** | Mirror specifications of the 600 mm ESAOT prototype.

Parameter	PM	DSM	FM
Profile	Concave paraboloid	Concave ellipsoid	Flat
Conic coefficient	-1.000	-0.466	-
Radius	-2040 mm	504.8 mm	Infinity
Clear aperture	$\Phi=590$ mm	$\Phi=174$ mm	56 mm $\times$ 78 mm (elliptical)
Coating	Protected aluminum	Protected silver	Protected silver

## Section 2: DSM and HS f-WFS design

The ESAOT prototype is designed for installation at the Lijiang observatory in Yunnan province, China (100°01'48"E, 26°41'42"N, 3200 m altitude). The site experiences atmospheric seeing conditions ranging from 0.5" to 5.5" at night, with a median daytime seeing of 1.16" (equivalent to an atmospheric coherence length  $r_0$  of 9.8 cm). Daytime seeing is worse due to solar radiation, with  $r_0$  varying from 11.5 cm in the morning to 1.5 cm at noon, and recovering to 6.0 cm in the afternoon<sup>S1</sup>.

In this study, the measured atmospheric coherence length ( $r_0$ ) data were analyzed and fitted. The median value of  $r_0$  was selected as the design basis for the DSM in the 600 mm ESAOT prototype system. As illustrated in Fig. S2, the fitted data indicate that the best and worst  $r_0$  values are approximately 9.75 cm and 0.75 cm, respectively, with a median value of about 4.5 cm. Based on the relationship between atmospheric coherence lengths at different wavelengths, the equivalent  $r_0$  at the TiO band was determined to be approximately 6.07 cm. This value serves as the design reference for both the HS f-WFS and the DSM in the 600 mm ESAOT system.

The DSM in the 600 mm ESAOT system features a discrete actuator configuration with a continuous face plate. Piezoelectric PZT is selected as the actuator material due to its fast response time and high precision. Based on the earlier research findings of Greenwood et al.<sup>S2</sup>, the number of DSM actuators required for effective atmospheric wavefront aberration correction, denoted as  $N_{act}$ , can be preliminarily estimated using the following relationship:

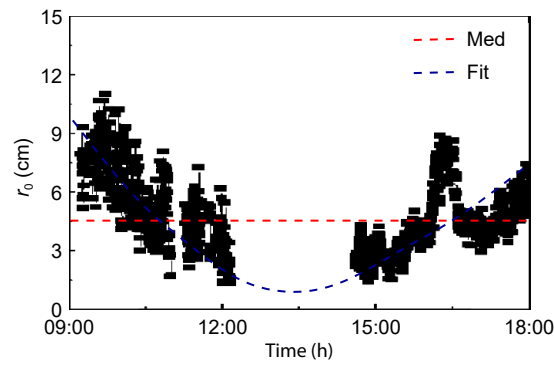


**Fig. S2** | Temporal variations of the atmospheric coherence length ( $r_0$ ) during daytime at Lijiang observatory. The blue dashed line represents the fitted data, while the red dashed line indicates the median value of  $r_0$ .

$$\sigma_{\text{fitting}}^2 = 0.274 \left( \frac{D}{r_0} \right)^{5/3} N_{\text{act}}^{-5/6}, \text{ rad}^2, \quad (1)$$

here,  $\sigma_{\text{fitting}}$  represents the fitting residual after atmospheric aberration correction by the DSM, which is required to be below  $0.1\lambda$ .  $D$  denotes the clear aperture of the ESAOT system, measuring 590 mm, and  $r_0$  is the equivalent atmospheric coherence length for the observation band.

Based on Eq. (6), it can be preliminarily determined that the number of DSM actuators,  $N_{\text{act}}$  should be larger than 60.95. In this system,  $N_{\text{act}}$  is set to 61, aligning with the typical number of actuators in a hexagonal distribution for deformable mirrors. The actuators are initially arranged uniformly across three concentric rings, including a central actuator, with 6, 18, and 36 actuators in the first, second, and third rings, respectively. However, the actuator distribution of the DSM will be further optimized for practical applications, as discussed in Section 3. DSM actuators travel up to  $\pm 5 \mu\text{m}$  allows re-correction of high frequency residual tip-tilt errors after Hexapod correction. Detailed design parameters of the DSM are provided in Table S3.

**Table S3** | Parameters on 61-DSM.

Parameter	Value
Aperture size	$\Phi=210 \text{ mm}$
Clear aperture	$\Phi=172 \text{ mm}$
Freedom of correction	61
Actuator layout	Annular
Actuator material	PZT
Actuator spacing	18.5 mm (~62.8 mm, mapping to PM)
Actuator stroke	$\pm 5 \mu\text{m}$
Coupling coefficient	~10%
Resonant frequency	Over 2000 Hz

The HS f-WFS is critical for accurate wavefront detection and correction. The 600 mm ESAOT prototype employs a cross-correlation HS f-WFS with a  $12 \times 12$  lenslet array, operating at a center wavelength of 550 nm with a 10 nm bandwidth. The sensor uses a high-speed CMOS detector (EoSens@CL) capable of 2000 fps, with each lenslet covering  $36 \times 36$  pixels and a resolution of around  $0.67''/\text{pixel}$ , suggesting a field of view (FoV) of around  $24'' \times 24''$ . The FoV of the HS f-WFS specifically denotes the sub-aperture image area used for cross-correlation-based slope calculations between sub-apertures, but not the telescope's observational coverage. A corresponding field stop is incorporated to prevent signal crosstalk between sub-apertures. Detailed HS f-WFS parameters are provided in Table S4.

**Table S4** | Parameters of the HS f-WFS.

Parameter	Value
Wavelength	550 nm (10 nm bandwidth)
Resolution	12×12 (96 valid)
Lenslet size	504 $\mu\text{m}$ × 504 $\mu\text{m}$
Field of View (FoV)	24" × 24"
Lenslet focal length	30 mm
Pixel resolution	36×36 (14 $\mu\text{m}$ pixels)
Frame frequency	900–2000 fps, adjustable

### Section 3: Experimental results

Static and dynamic wavefront correction experiments were conducted to evaluate the system's performance. The results demonstrate that static wavefront aberrations were significantly reduced from  $5.1\lambda$  (peak-to-valley, PV) and  $0.95\lambda$  (root-mean-square, RMS) to  $0.33\lambda$  (PV) and  $0.06\lambda$  (RMS) after correction by the deformable secondary mirror (DSM). Additionally, dynamic tracking errors were reduced by factors of 14.3 and 5.3 in the  $X$  and  $Y$  directions, respectively, with a correction bandwidth of approximately 30 Hz.

Figure S3 presents the wavefront aberration detected by the HS f-WFS and the corresponding residual wavefront error compared to a simulated random phase screen. The detected wavefront aberration closely matches the given random phase screen, with minor discrepancies attributed to the HS f-WFS's limited ability to resolve high spatial frequency components and the spatial filtering effect of using the first 65 orders of Zernike polynomials. As shown in Fig. S3(a), the peak-to-valley (PV) and root-mean-square (RMS) values of the detected wavefront are  $2.56\lambda$  and  $0.48\lambda$ , respectively.

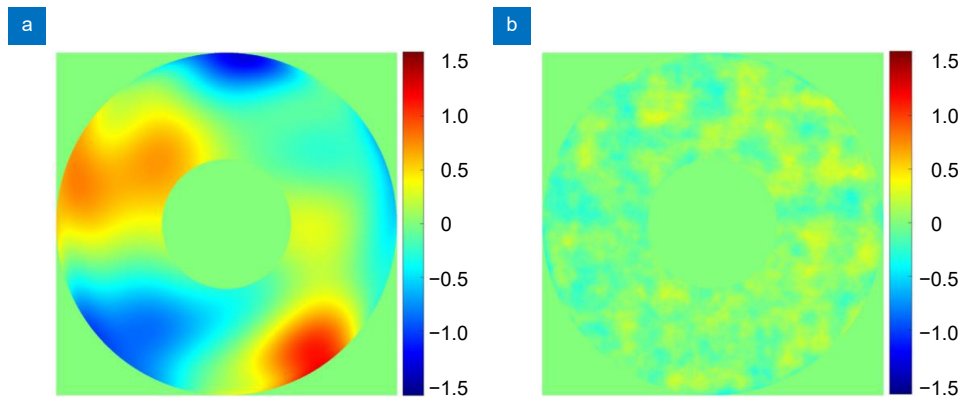


**Fig. S3** | Wavefront detection by the HS f-WFS and its residual wavefront error. (a) Phase distribution of wavefront aberration detected by HS f-WFS, with a PV value of  $2.56\lambda$  and a RMS value of  $0.48\lambda$ . (b) Residual wavefront error compared to the given random phase screen, showing a PV of  $0.73\lambda$  and a RMS of  $0.12\lambda$ .

The measured wavefront slopes from the HS f-WFS were input into the ESAOT controller, which calculated and output the corresponding correction voltage values to the DSM. The resulting DSM surface shape after wavefront correction and the corresponding residual wavefront error are shown in Fig. S4. Compared to the initial wavefront, the DSM surface exhibits a relatively smooth profile, reflecting its limited ability to correct high-frequency aberrations. As a result, the residual wavefront error primarily consists of high-frequency components. Nevertheless, the overall root-mean-square (RMS) value of the corrected wavefront is reduced to below  $0.10\lambda$ , demonstrating the system's effectiveness in wavefront correction.

During the wavefront correction process, image quality was significantly influenced by wavefront aberrations. To assess this impact, the structural similarity index (SSIM)<sup>S3</sup> was employed to quantify image quality before and after DSM correction. The original image, serving as the reference, has an SSIM of 1.0. As wavefront aberrations diminish after DSM correction, the SSIM value approaches 1.0, indicating enhanced image quality.

In simulations, the original image of the solar atmospheric photosphere, with a field of view (FoV) of approximately

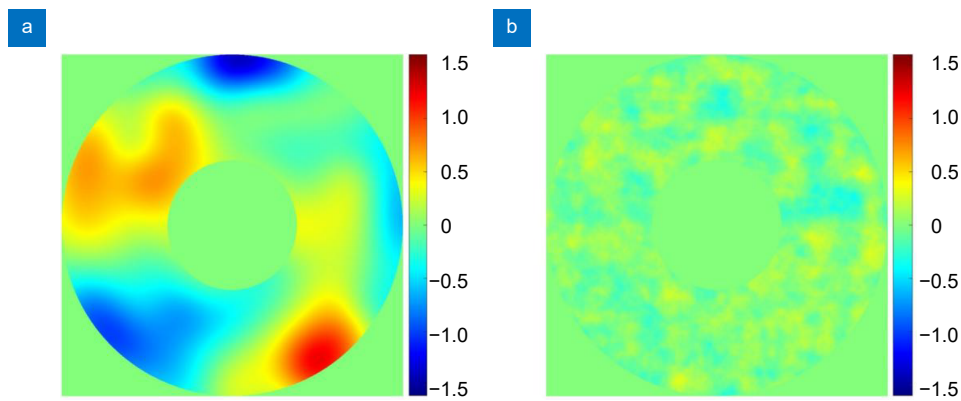


**Fig. S4** | DSM profile and the corresponding residual wavefront error after wavefront correction. (a) Shape of DSM after wavefront correction ( $PV=2.65\lambda$ ,  $RMS=0.47\lambda$ ). (b) The corresponding residual wavefront error after correction ( $PV=0.72\lambda$ ,  $RMS=0.10\lambda$ ).

66", was generated by Dr. Carlos Quintero Noda, as shown in Fig. S5(a). The diffraction-limited image, depicted in Fig. S5(b), was obtained by convolving the original image with the ideal point spread function (PSF) of the 600 mm ESAOT

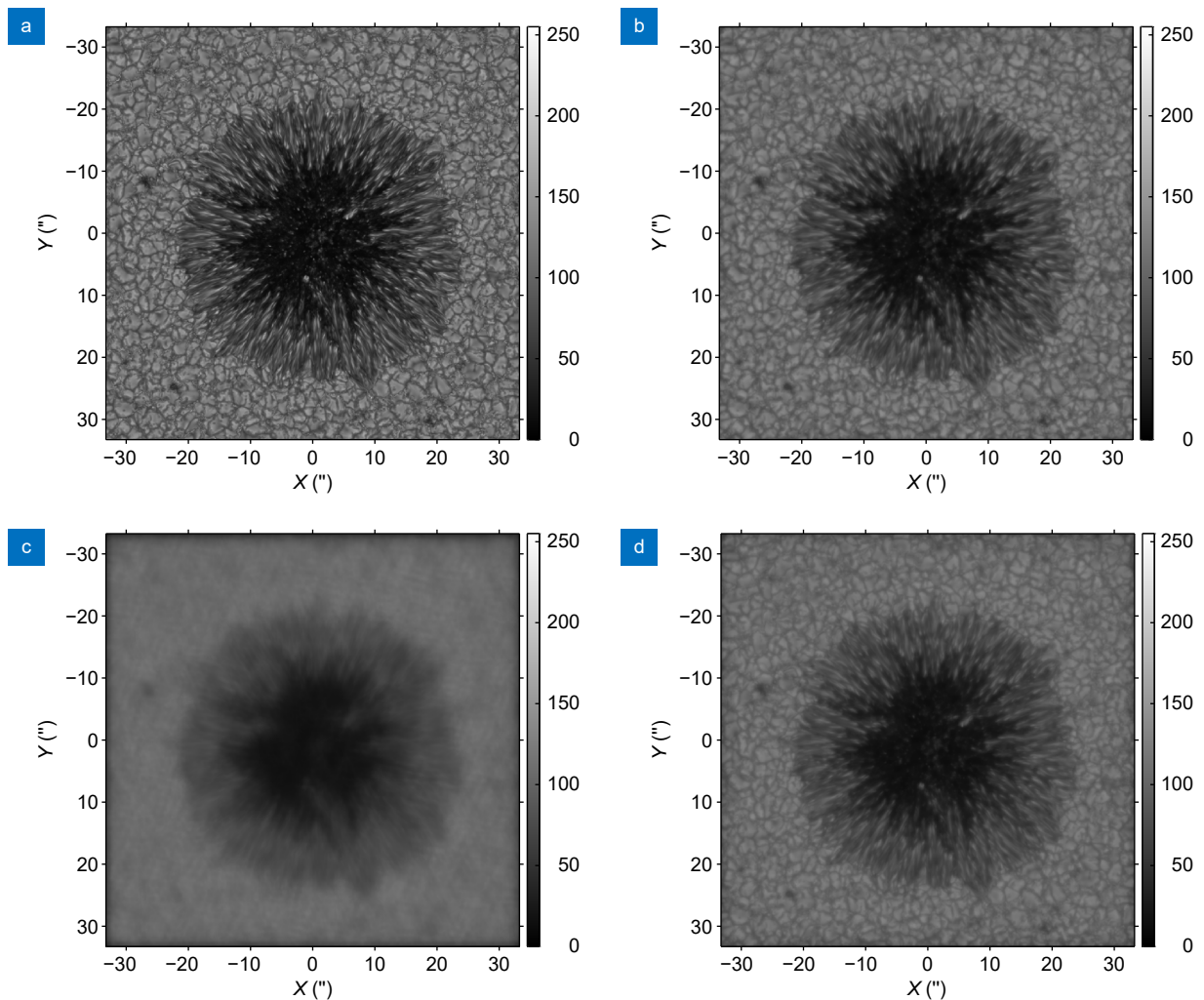
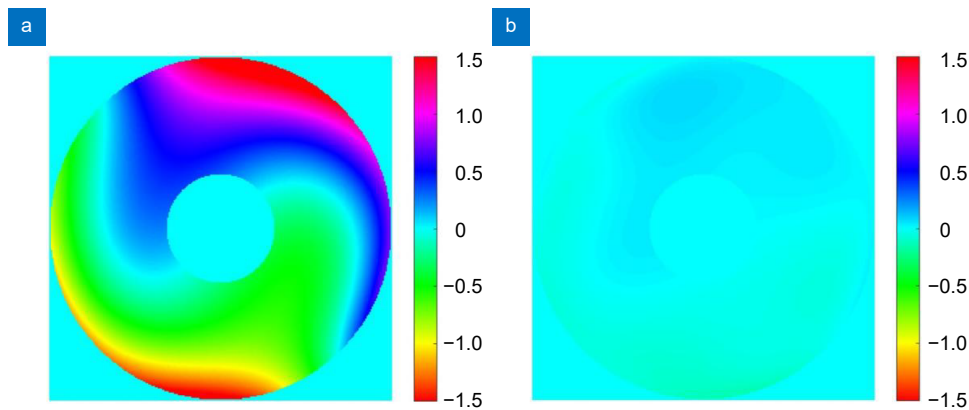


**Fig. S5** | Images of original, diffraction-limited, and wavefront-corrected scenarios. (a) Original image of the solar photosphere layer, used as the reference image ( $SSIM=1.0$ ). (b) Diffraction-limited image of (a), constrained by the ideal point spread function (PSF) of the 600 mm ESAOT system ( $SSIM=0.7817$ ). (c) Image degraded by atmospheric turbulence before wavefront correction ( $SSIM=0.269$ ). (d) Image after wavefront correction, demonstrating improved quality ( $SSIM=0.6891$ ).

system, yielding an SSIM of 0.7817. Under atmospheric turbulence, the SSIM dropped to 0.2690 before correction but improved to 0.6891 after DSM correction, as illustrated in Fig. S5(c) and S5(d), respectively. In the current simulation, we mainly focused on atmospheric turbulence effects under an isoplanatic assumption and did not include non-isoplanatic error analysis.

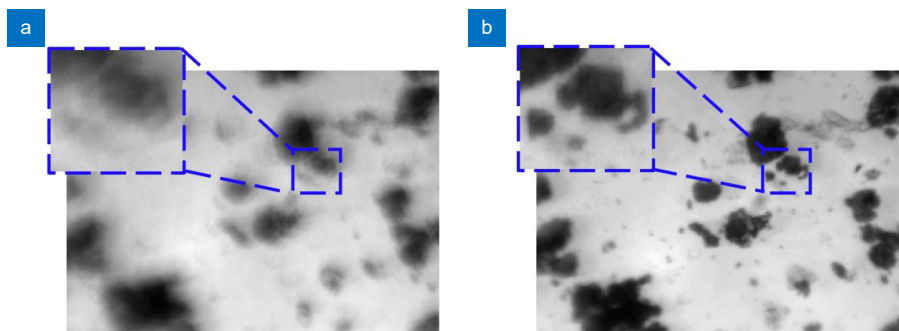
The correction capability for static wavefront aberrations was validated first. The simulated static wavefront aberrations primarily arose from misalignment between the DSM and downstream optics adjusted by the Hexapod mechanism, as well as shape changes in the DSM itself. A  $12 \times 12$  resolution Hartmann-Shack wavefront sensor (HS WFS) was developed to detect these simulated wavefront aberrations. The collected data were fed into the real-time controller (RTC) to adjust the DSM's shape. Wavefront detection, control, and correction were performed for both point and extended objects.

The wavefront aberrations of the experimental system before and after DSM correction are shown in Fig. S6. The simulated static wavefront aberrations were dominated by the first 15 Zernike modes, with a PV value of  $3.59 \mu\text{m}$  ( $5.1\lambda$ ) and a RMS value of  $0.67 \mu\text{m}$  ( $0.95\lambda$ ) at the working wavelength. After DSM correction, the residual wavefront error was significantly reduced to a PV of  $0.23 \mu\text{m}$  ( $0.33\lambda$ ) and a RMS of  $0.04 \mu\text{m}$  ( $0.06\lambda$ ). These results validate the DSM's effectiveness in correcting static wavefront aberrations.



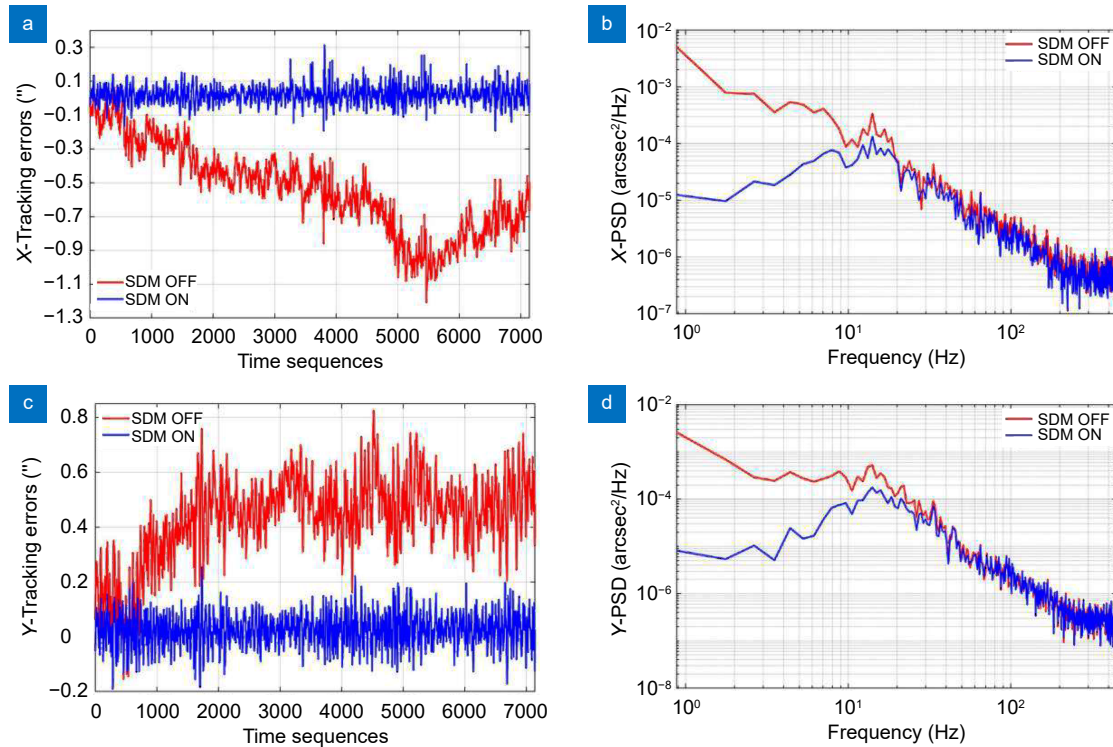
**Fig. S6** | Wavefront correction performance. (a) Initial wavefront aberration before DSM correction, with a PV value of approximately  $5.1\lambda$  and a RMS value of  $0.95\lambda$ . (b) Residual wavefront error after DSM correction, showing a PV of approximately  $0.33\lambda$  and an RMS of  $0.06\lambda$ .

Figure S7 depict images of the simulated extended light source captured by the camera before and after wavefront correction. The results demonstrate a significant improvement in image quality for extended objects following wavefront aberration correction. After DSM correction, the imaging contrast of the simulated extended target increased by a factor of 1.72.



**Fig. S7** | Experimental images of the simulated extended light source. (a) Image before wavefront correction. (b) Image after wavefront correction, showing an improvement in imaging contrast by approximately 1.72 times.

Figure S8 illustrate dynamic tracking curves and power spectral density (PSD) of the 600 mm ESAOT prototype along the X and Y directions before and after DSM correction. The results demonstrate a significant reduction in tracking error. Specifically, the tracking error in the X direction decreased from a maximum of 1" before correction to approximately  $\pm 0.07''$  after correction, improving tracking accuracy by a factor of 14.3 (Fig. S8(a)). Similarly, the tracking error in the Y direction was reduced from a maximum of 0.8" before correction to  $\pm 0.15''$  after correction, achieving a 5.3-fold improvement in accuracy (Fig. S8(c)). Figure S8(b) and S8(d) present the PSD curves of the tracking error along the X and Y directions before and after DSM correction. Based on the analysis, the correction bandwidth for skew errors is estimated to be approximately 30 Hz.



**Fig. S8** | Tracking error before and after DSM correction. (a) Tracking error in the X direction. (b) Power spectral density (PSD) of the tracking error in the X direction. (c) Tracking error in the Y direction. (d) PSD of the tracking error in the Y direction.

## References

- S1. Shumko S, Gorceix N, Choi S et al. AO-308: the high-order adaptive optics system at big bear solar observatory. *Proc SPIE* **9148**, 914835 (2014).
- S2. Greenwood DP. Mutual coherence function of a wave front corrected by zonal adaptive optics. *J Opt Soc Am* **69**, 549–553 (1979).
- S3. Wang Z, Bovik AC, Sheikh HR et al. Image quality assessment: from error visibility to structural similarity. *IEEE Trans Image Process* **13**, 600–612 (2004).